

Stability of Anomalous Hall Crystals in multilayer rhombohedral graphene

Zhihuan Dong, Adarsh S. Patri, and T. Senthil

Department of Physics, Massachusetts Institute of Technology, Massachusetts 02139, USA
(Dated: March 13, 2024)

Recent experiments showing an integer quantum anomalous Hall effect in pentalayer rhombohedral graphene have been interpreted in terms of a valley-polarized interaction-induced Chern band. The resulting many-body state can be viewed as an Anomalous Hall Crystal (AHC), with a further coupling to a weak moiré potential. We explain the origin of the Chern band and the corresponding AHC in the pentalayer system. We propose a simplified model that focuses on the physics near high symmetry Brillouin zone points to describe the competition between AHC and Wigner Crystal (WC) phases. We discuss the possible role of the moiré potential. We emphasize that even if in the moiré-less limit, the AHC is not favored over a correlated Fermi liquid, the moiré potential will push the system into a ‘moiré-enabled AHC’. We also suggest that there is a range of alignment angles between R5G and hBN where a $C = 2$ insulator may be found at integer filling.

I. INTRODUCTION

In the last few years, the Integer Quantum Anomalous Hall (IQAH) effect has been seen in a number of moiré materials^{1–6}. Microscopically, typically, the electronic bands of many of these moiré materials have a well-defined Chern number that is equal and opposite in the two valleys. When the bands are nearly flat, and the total number of electrons is an odd integer per moiré unit cell, the valley (and spin, if present) degree of freedom polarizes spontaneously^{7–10}, leading to an insulating ground state with a net Chern number for occupied bands, and hence to an IQAH effect.

The recent discovery¹¹ of the IQAH (and a Fractional Quantum Anomalous Hall (FQAH)) state in pentalayer rhombohedral graphene (R5G) nearly aligned with a hexagonal Boron-Nitride substrate (R5G/hBN) does not fit this paradigm. Rather, the non-interacting band structure is such that, even with spin and valley polarization, the many-body state is metallic at a filling $\nu = 1$ of the moiré lattice. However, electron-electron interaction effects, treated in a Hartree-Fock approximation^{12–15}, lead to the appearance of a single-particle gap, and an insulating many-body ground state (see also Ref. 16). The occupied Hartree-Fock band has a non-zero Chern number $|C| = 1$ which provides an explanation for the observed IQAH at $\nu = 1$. Furthermore, numerical calculations^{12–15} of the many-body state at fractional filling, by considering the Coulomb interaction projected to the $\nu = 1$ Hartree-Fock band, find fractional quantum Hall states in general agreement with the FQAH found in the experiment. The physics of the QAH in pentalayer graphene is thus quite different from the twisted Transition Metal Dichalcogenide (tTMD) system MoTe₂ where the first discovery of the FQAH was made^{17–20}.

In this paper, we focus on the IQAH state and provide a deeper understanding of the emergence of the interaction-induced Chern band at $\nu = 1$. We will mostly limit ourselves to the Hartree-Fock approximation, and explain why the Chern band is stabilized. We will show that there is a range of alignment angles for which the

non-interacting band already has Berry curvature close to 2π . In this regime, with interactions, the Fock term dominates and both opens up a band gap and modifies the integrated Berry curvature to be exactly 2π to yield a $C = 1$ Chern insulator. As the alignment angle is reduced (toward the one in the devices of the experiments of Ref. 11), the net Berry curvature of the non-interacting model within the first Brillouin zone decreases to well below 2π . In this regime, the Fock term is not enough to stabilize a $C = 1$ insulator. However we show that the combination of Hartree and Fock terms suffice, and we explain the associated physics. Briefly, in this regime of alignment angles, the Fock term opens up a band gap and gives an insulator. However, the stabilization of the $C = 1$ insulator over the $C = 0$ one is due to the Hartree term. This is roughly because the charge distribution in the Chern insulator is more homogenous than the trivial insulator due to the impossibility of strongly localizing the electrons in a Chern band.

It was noted in Ref. 13 and 14 (and reproduced in our own calculations) that the Hartree-Fock calculation produces a Chern insulator even in the absence of an explicit moiré potential. A natural interpretation is that the continuous translation symmetry, present in the absence of the moiré potential, is spontaneously broken to form some kind of crystalline state. However, since the Hartree-Fock description of the crystal has occupied bands with a net Chern number, this state should be viewed as an ‘Anomalous Hall Crystal’²¹ (AHC). The moiré potential will, at the very least, pin the AHC. From this point of view, our results can be viewed as an explanation (within Hartree-Fock) for what stabilizes the AHC over either an ordinary Wigner crystal (WC) or a Fermi liquid (FL) metal.

To capture the competition between the AHC and the WC in rhombohedral n -layer graphene (RnG), we propose a complementary simplified model that focuses on the symmetry indices at the MBZ corners K_M and \bar{K}_M , in the spirit of a ‘Landau’ theory. The ground state energy, expressed as a function of these indices, contains the key information about the AHC - WC competition.

The evolution between the Fermi liquid metal and the ordinary Wigner crystal is, of course, one of the classic problems in condensed matter physics. In the context of RnG, the Hall crystal is another possible phase. It is well known that the phase competition between the Fermi liquid and the ordinary Wigner crystal is very poorly described by Hartree-Fock theory which enormously overestimates the stability of the crystal. We might expect that a similar situation also arises in RnG with the crystalline phases (AHC or WC) much less stable than indicated by Hartree-Fock theory. However, we suggest that even a very small moiré potential can induce a phase transition between a correlated Fermi liquid and the Hall crystal as the latter gains commensuration energy. Thus, we expect the Hartree-Fock calculation to be more reliable in the presence of moiré than without. We dub the resulting IQAH state a ‘moiré-enabled Anomalous Hall Crystal’. Obviously, in the regime of the moiré-enabled AHC, if we turn off the moiré potential, the system is a Fermi liquid. In this situation, the moiré potential is important in getting into the AHC state (through a first-order transition out of the Fermi liquid), but ultimately the gap in the AHC is determined by the Coulomb interaction and not by the amplitude of the periodic potential. We comment on some implications of this possibility.

We also consider the possibility of obtaining interaction-induced Chern bands with higher Chern numbers. Indeed the naive expectation about RnG/hBN is that, for the topologically non-trivial orientation of the displacement field, the bands have (valley) Chern number n . Though this expectation is not borne out¹, there is a large Berry curvature in the non-interacting band that is peaked in a ring in momentum space. The size of the ring is set by the displacement field. Thus, with increasing twist angle, a greater portion of this Berry curvature will sit inside the moiré Brillouin zone. Then, if interactions open up a band gap at moiré filling $\nu = 1$, we might expect a filled band with a higher Chern number. Complicating this expectation, the non-interacting dispersion loses its flatness also at the location of the ring. Hence, a detailed calculation is required. We will show, within the Hartree-Fock approximation for R5G/hBN, that if the strength of the moiré potential or the Coulomb interaction strength can be tuned, then $C > 1$ insulators may be obtained at $\nu = 1$, which then raises the possibility of exploring the physics at fractional filling of a higher Chern band. Previously a $C = 2$ QAH state was found¹ in R3G/hBN at $\nu = 1$ of the valence band, and a $C = 5$ insulator at neutrality in spin-proximitized R5G at neutrality²².

The remainder of the paper is organized as follows. In Sec. II we describe the continuum models for R5G, and highlight the limitations of a simple and popular two-band model. Specifically, it fails to capture the realistic Berry curvature distribution at small momentum, which is critical to our understanding of the AHC. We next overview the features of the Hartree-Fock phase diagram in Sec. III, for varied twist angles and displace-

ment field energies, and provide an understanding for the interaction-driven Chern bands. We next detail the mechanism by which the AHC is favored over the trivial WC in Sec. IV through a careful consideration of the symmetry indices at high-symmetry points of the mini-Brillouin zone. We also provide a complementary argument in Sec. V via a Ginzburg-Landau-like effective model. In Sec. VI, we discuss the competition of the AHC and the Fermi liquid state in the moiré-less setting within Hartree-Fock. In Sec. VII, we discuss features of the phase diagram beyond the Hartree-Fock approximation, and comment on the fate of both the moiré and non-moiré system depending on the interactions and displacement field. We emphasize the presence of a moiré-enabled AHC which expands (likely vastly) the relevance of the physics of the AHC in the phase diagram. In Sec. VIII we discuss possible routes for higher Chern bands. Finally, we conclude in Sec. IX and provide some future directions of exploration.

II. STRUCTURE OF CONTINUUM BAND AT LARGE DISPLACEMENT FIELD

Rhombohedral-stacked pentalayer graphene is the structure formed by five layers of graphene vertically aligned in the $(ABCAB)$ sequence, with the B_l sublattice of layer l aligned with the A_{l+1} sublattice of layer $l + 1$. The continuum 10-orbital Hamiltonian (in the basis of the A_l, B_l sublattices for each of the five layers; for a given valley K/K' and spin \uparrow/\downarrow) involves tunneling of Dirac fermions from each graphene monolayer (with Dirac velocity γ_0) to neighboring layers via hopping processes $t_{1,2,3,4}$ (see Eq. A1 in Appendix A) in the presence of on-site potentials and displacement field energies (u_d)²³. We present in Fig. 1 and Fig. 2 the (conduction) continuum band structure, and the associated Berry curvature and flux of the 10-band model.

The hierarchy of energy scales associated with the inter-layer hopping processes is $t_1 > t_{3,4} \gg t_2$. This indicates the important role of t_1 in the low-energy theory. To develop an intuitive low-energy description of this continuum model, and its corresponding non-trivial topology, it is advantageous to consider various effective models that are applicable in different momenta regimes.

We will drop the moiré potential in our discussion of the Hartree-Fock calculation, and develop an understanding of the stabilization of the AHC as a function of the electron density and the displacement field. We find it convenient to parametrize the electron density in terms of the alignment angle θ with the hBN substrate (even though we turn off the moiré potential). If the moiré potential were to be present, the twist angle θ determines the size of the unit cell. The charge density of interest corresponds to a lattice filling $\nu = 1$ of this unit cell. Consequently, θ can be used as a parametrization of the density even in the absence of moiré.

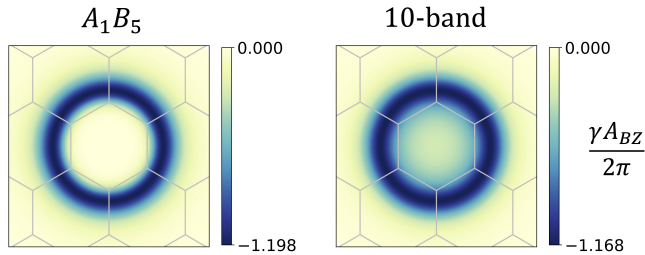


Figure 1. Berry curvature distribution for (a) the 2-orbital (A_1B_5) model, and (b) the 10-orbital model without warping ($t_2 = t_3 = t_4 = 0$), at $u_d = -35\text{meV}$. We mark the edge of MBZ at $\theta = 0.8^\circ$ with silver lines, although no moiré potential is turned on in the calculation.

A. Dangling edges of pentalayer graphene: k^5 -two-orbital model

A preliminary understanding of the continuum band near charge neutrality is achieved by focusing on the electronic occupation of the A_1 and B_5 orbitals. The remaining eight orbitals are regarded as high-energy sites, with a low-energy model derived from perturbatively integrating out these high-energy orbitals²³. The justification for this simplified model is that at small momentum k , $\gamma_0 k/t_1 \ll 1$, and so the dominating interlayer hopping t_1 pushes all other orbitals away from zero energy by forming bonding and anti-bonding states so that the only low energy degrees of freedom are A_1 and B_5 orbitals. The effective low energy theory is obtained by performing a fifth-order perturbation with small in-plane hopping $\gamma_0 k$, leading to the effective model²³⁻²⁵,

$$H = \begin{bmatrix} 2u_d & \frac{\gamma_0^5}{t_1^4}(k_x + ik_y)^5 \\ \frac{\gamma_0^5}{t_1^4}(k_x - ik_y)^5 & -2u_d \end{bmatrix}. \quad (1)$$

We note that we disregard the sub-dominant hopping momentum corrections that involve lower powers of momentum k . This theory defines two momentum regimes:

- (1) $\frac{u_d^{1/5} t_1^{4/5}}{\gamma_0} \ll k \ll \frac{t_1}{\gamma_0}$, where the off-diagonal term dominates, which leads to a $\sim k^5$ dispersion; and
- (2) $k \ll \frac{u_d^{1/5} t_1^{4/5}}{\gamma_0}$, where the displacement field dominates, corresponds to an extremely flat band bottom (dictated by u_d) with a $\sim k^{10}$ dispersion.

The distribution of the Berry curvature associated with this two-band model is given by,

$$\gamma(k) = -\frac{25u_d(t_1^{4/5}/\gamma_0)^8 k^8}{\left[(t_1^8/\gamma_0^{10})k^{10} + 4u_d^2\right]^{3/2}}. \quad (2)$$

Indeed, the corresponding total Berry flux is -5π within the first Brillouin zone (though there is no gap), which is distributed in a ring-like region about $k = 0$ (see Fig. 1(a)). The radius of this ring is given by the tran-

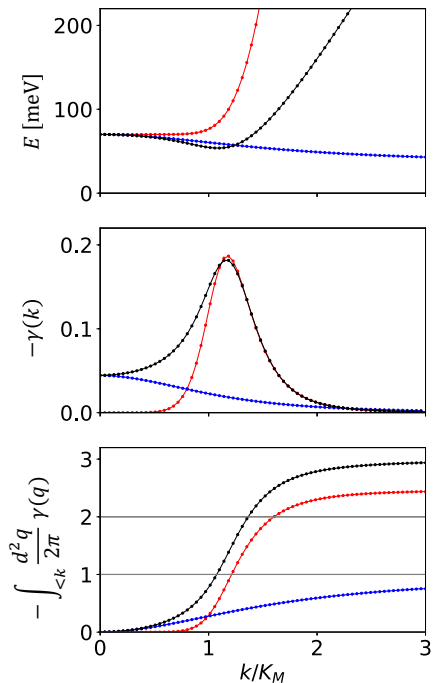


Figure 2. Dispersion (top), Berry curvature distribution (middle), and Berry flux integral (bottom) for various effective models of pentalayer graphene. Black, red, and blue curves correspond to 10-band (Eq. A1 in Appendix A), 2-band (Eq. 1), and 3-band models (Eq. 3), respectively. This plot is obtained for $u_d = -35\text{meV}$, and $\theta = 0.9^\circ$.

sition momentum scale $k_{ring} \sim \frac{u_d^{1/5} t_1^{4/5}}{\gamma_0}$, where the band starts to become highly dispersive.

In the presence of the moiré potential, there is another momentum scale, which depends on the twist angle θ . We will characterize it with K_M the momentum at the corner of the moiré Brillouin zone (MBZ). At the range where the IQAH is observed in current experiments ($\theta \sim 0.77^\circ$, $u_d \sim -35\text{meV}$) k_{ring} is slightly above K_M (as seen in Fig. 1(a)). This indicates that the majority of the Berry curvature arising from the $A_1 - B_5$ hybridization lies outside the first MBZ.

B. Failure of k^5 -two-orbital model to capture flat band bottom

The limitation of the k^5 -two-orbital model is brought to the fore as the displacement field energy increases. We recall from the above discussion that at relatively weak displacement field energies ($|u_d| < 10\text{meV}$) and momenta, the band bottom is relatively flat. As such, the k^5 -two-orbital model (in regime (2)) faithfully captures the features of the 10-orbital model. As the displacement field increases (see Fig. 2) and the flat-band region expands to envelop the size of the moiré BZ, the band-bottom (i.e. near $k = 0$) acquires an appreciable dispersion. This appreciable dispersion is missed by the above

simplistic two-orbital model. To see this, one notices that the hybridization between B_5 and B_4 is linear in k (see the 10-orbital model in Eq. A1 in Appendix A) and can become much stronger than the effect of the k^5 term at small k . Therefore, it is more appropriate to begin with the Hamiltonian projected to include this nearest orbital i.e. in the B_5 , A_5 , and B_4 orbitals²⁶

$$H_3 = \begin{bmatrix} 2u_d & \gamma_0(k_x + ik_y) & 0 \\ \gamma_0(k_x - ik_y) & 2u_d & t_1 \\ 0 & t_1 & u_d \end{bmatrix}. \quad (3)$$

Diagonalizing this Hamiltonian in the limit of small k and dominating t_1 , we find the eigenstates: $|B_5\rangle, |A_5B_4^+\rangle = \frac{1}{\sqrt{2}}(|A_5\rangle + |B_4\rangle)$, and $|A_5B_4^-\rangle = \frac{1}{\sqrt{2}}(|A_5\rangle - |B_4\rangle)$. Written in this eigenbasis basis, the Hamiltonian becomes

$$\tilde{H}_3 = \begin{bmatrix} 2u_d & \frac{\gamma_0(k_x + ik_y)}{\sqrt{2}} & \frac{\gamma_0(k_x + ik_y)}{\sqrt{2}} \\ \frac{\gamma_0(k_x - ik_y)}{\sqrt{2}} & t_1 + \frac{3u_d}{2} & \frac{u_d}{2} \\ \frac{\gamma_0(k_x - ik_y)}{\sqrt{2}} & \frac{u_d}{2} & -t_1 + \frac{3u_d}{2} \end{bmatrix} \quad (4)$$

At $k = 0$, the lowest conduction band state is $|\psi^0\rangle = (1, 0, 0) = |B_5\rangle$, as expected. For small k , the k -dependent matrix elements can be treated within perturbation theory. The leading correction to the eigenstate of the lowest conduction band is,

$$\begin{aligned} |\delta\psi_1\rangle &= -\frac{\gamma_0 k^*}{2} \left(\frac{u_d}{t_1^2 - u_d^2/4} |A_5\rangle + \frac{2t_1}{t_1^2 - u_d^2/4} |B_4\rangle \right) \\ &\sim -\frac{\gamma_0 k^*}{t_1} |B_4\rangle \end{aligned} \quad (5)$$

and its corresponding energy correction is,

$$\delta E_2 = -\frac{\gamma_0^2 |k|^2}{2} \left(\frac{1}{t_1 - u_d/2} - \frac{1}{t_1 + u_d/2} \right) \sim -\frac{u_d \gamma_0^2 |k|^2}{2t_1^2}. \quad (6)$$

The leading correction to the dispersion in Eq. 6 suggests a negative effective mass that scales with displacement field. As such, the band bottom is not as flat in the large displacement field energy as the k^5 -two-orbital model would seem to indicate. We present in Fig. 2 the conduction band bottom dispersion for the k^5 -two-orbital model and the above perturbation theory modified effective three-orbital model (with the 10-orbital model's dispersion shown for comparison). As seen, the k^5 -two-orbital model is 'too flat' in the small momentum region; the effective three-orbital has the required dispersion, consistent with the full 10-orbital model.

In addition to the modified dispersion, the correction to the $|B_5\rangle$ eigenstate by Eq. 5 indicates that the Berry curvature in the small k -regime resembles that of a massive Dirac cone. This entails a Berry phase of approximately $-\pi$ distributed in the small region of $k \sim t_1/\gamma_0$. This is corroborated by the full 10-orbital model, where γ_{BZ} , the Berry flux inside the MBZ, is slightly stronger than $-\pi$ (see Fig. 2); recall that at the larger displacement fields discussed here, the 'ring' of Berry curvature

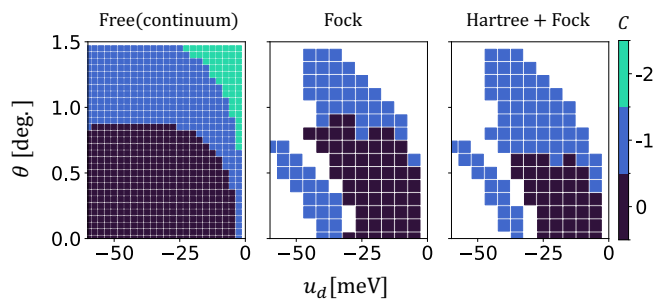


Figure 3. Phase diagrams in $\theta - u_d$ space. In (a) The colors show the closest integer to $\gamma_{BZ}/2\pi$, where γ_{BZ} is defined in the main text. Colors in (b) and (c) mark the Chern number of mean field bands, obtained with Fock term only and full Hartree-Fock, respectively. Here the metallic region is left uncolored. Comparing (a) and (b), the boundary between $C = 0$ and $C = -1$ region in the Fock phase diagram closely tracks that of the non-interacting phase diagram. The comparison between (b) and (c) shows that the Hartree term extends the stability of the $C = -1$ Hall crystal. These results are obtained for the 10-orbital model with no warping term, and with the moiré potential turned off. The angle θ should then be viewed as a parametrization of the charge density.

lies just outside the MBZ. While the ring-shaped feature at larger momentum arising from $B_5 - A_1$ mixing also contributes to γ_{BZ} , the described $-\pi$ flux is predominantly due to the massive Dirac cone physics at small k due to $B_5 - B_4$ mixing. In the following section, we will see that this massive Dirac cone feature is crucial since the γ_{BZ} of the non-interacting band, to a large extent, determines the Hartree-Fock phase diagram.

III. UNDERSTANDING THE HARTREE-FOCK PHASE DIAGRAM

In this section, we overview the phenomenology of the mean-field findings of pentalayer graphene and explain the physics for some parts of the phase diagram. In particular, we focus on the conduction band in the regime of strong displacement field ($u_d \sim -35\text{meV}$) relevant to current experiments on R5G. We consider the evolution as twist angle θ (i.e. the charge density) decreases, and ignore the moiré potential. The Hartree-Fock and Fock phase diagrams are shown in Fig. 3²⁷. We focus on a simplified model with no warping $t_2 = t_3 = t_4 = 0$; the warping effects are readily included and do not affect the physical understanding we develop.

Extremal twist angle $\theta > 1.5^\circ$: In this limit, $K_M > k_{ring}$, and so the majority of the continuum band Berry curvature is contained within the first MBZ. We recall that k_{ring} also marks the momentum scale at which the continuum band becomes dispersive. As a result, given that the band gap opening at the mean-field level is bounded (from above) by the scale of interaction

$U \sim 20\text{meV}$, the energy of the second conduction band at the M_M point may drop well below the energy of the first conduction band at K_M , which leads to a metallic phase even when the translation symmetry is spontaneously broken.

Large twist angle $0.9^\circ < \theta < 1.5^\circ$: In this case, where the twist angle is larger than the experimental regime, the MBZ boundary intersects the Berry curvature ring, where the -5π Berry flux is concentrated. We find the Berry flux enclosed by the first MBZ varies between -3π and $-\pi$ as θ decreases. With Fock term alone turned on, the band gap opens, and we find the lowest conduction band has $C = -1$, which is exactly the Chern number expected from rounding $\gamma_{BZ}/2\pi$ to its closest integer. The inclusion of the Hartree term does not modify the result qualitatively.

We note that in this regime an AHC with a higher Chern number is potentially possible. For this to happen, we need the twist angle to be large enough to enclose more than -3π flux, but at the same time not so large that the band becomes too dispersive to be gapped out by interaction. Whether or not such a higher Chern AHC exists then depends on details of the model. Within the current simplified model, no $|C| > 1$ phase is observed in Fig. 3(c). Nonetheless, it is conceivable that some modification to the non-interacting model parameters (such as including trigonal warping, or tuning the strength of the Coulomb interaction) can favor the higher Chern AHC. In addition, we can also contemplate tuning the strength of the moiré potential to stabilize an interaction-induced higher Chern band. We will explore these phenomena in Sec. VIII.

Intermediate twist angle $0.6^\circ < \theta < 0.9^\circ$: This is the regime most relevant to existing experiments¹¹. Due to the smaller MBZ, the enclosed Berry flux in the first BZ is less than $-\pi$. With the Fock term alone, we find a trivial insulator (Wigner crystal), consistent with the smaller Berry flux in the non-interacting band structure. However, with the inclusion of the Hartree term, the $C = -1$ Hall crystal state is once again favored (as seen in Fig. 3). We emphasize that this Hall crystal state is not a straightforward expectation from the non-interacting theory. In Sec. IV, we will describe a mechanism, according to which the Hartree term generically (for various displacement fields, number of graphene layers, etc.) favors $|C| = 1$ Hall crystals at a moderate interaction strength (strong enough to gap out the band, but not as strong compared to the dispersion in higher MBZs, which is the regime most relevant to the experiments).

Small twist angle $\theta < 0.6^\circ$: Finally, at a very small twist angle, the MBZ is shrunk significantly and is unable to enclose any substantial Berry curvature. As a result, the low energy degrees of freedom in the continuum band are almost entirely trivial and featureless i.e. the Bloch function is almost completely polarized to $|B_5\rangle$. With the spontaneous breaking of translational symmetry, a

Wigner crystal develops.

Small θ and higher displacement field $|u_d| > 40\text{meV}$: At a small twist angle, the ring-like feature is in the second MBZ. Naively one may conclude that the Chern number will be zero since $|\gamma_{BZ}| < \pi$. However, the situation is more subtle as seen in Fig. 3(c). According to Eq. 6, a large displacement field leads to strong negative dispersion at small k . As a result, the lowest conduction band is now mainly formed by the second MBZ, which contains a significant part of the Berry curvature “ring”. Then the Berry flux in the second MBZ may well be close to -2π , which will get quantized to -2π when the Fock term is turned on. So a $C = -1$ band is again expected at the level of the mean-field calculation.

IV. SYMMETRY INDEX AND DENSITY PROFILE OF BLOCH FUNCTION

The prevalence of the $|C| = 1$ AHC in the phase diagram of Fig. 3 warrants an explanation for the mechanism by which the Coulomb interaction favors $|C| = 1$ AHC over $C = 0$ WC.

We begin with the “large twist angle” regime, where the Fock term by itself is sufficient to drive a $C = -1$ AHC. For this regime, our reasoning for the stabilization of AHC is relatively straightforward. The Berry phase γ_{BZ} is between $-\pi$ and -3π , which gets quantized to -2π when interaction is turned on to open a band gap. In the following, we describe the intuition for the Fock term to round $\gamma_{BZ}/2\pi$ to its closest integer. First, in this setup, due to the steep dispersion in higher MBZs, the hybridization due to interaction is only prominent close to the zone boundary, where the bands associated with \mathbf{k} and $\mathbf{k} + \mathbf{G}$ may come close in kinetic energy (\mathbf{G} is a reciprocal lattice of the AHC or WC). Therefore, the modification of the Berry curvature in the renormalized band will be concentrated on the zone boundary. Consider a scenario where the Chern number of the renormalized band is far away from $\gamma_{BZ}/2\pi$. / Then, sharp Berry curvature peaks must show up near the zone boundary in order to accommodate the additional Berry flux $2\pi C - \gamma_{BZ}$ in this narrow region. As is known from the trace inequality for Bloch bands, the magnitude of the Berry curvature at any k -point provides a lower bound on the trace of the quantum metric $g_{\mu\nu}$.

To see its effects, consider the Fock contribution to the mean field energy,

$$E_{Fock} = - \sum_{\mathbf{k}, \mathbf{k}', \mathbf{G}} V_{\mathbf{k}+\mathbf{G}-\mathbf{k}'} \lambda_{\mathbf{k}+\mathbf{G}, \mathbf{k}'} \lambda_{\mathbf{k}'-\mathbf{G}, \mathbf{k}} \langle c_{\mathbf{k}}^\dagger c_{\mathbf{k}+\mathbf{G}} \rangle \langle c_{\mathbf{k}'}^\dagger c_{\mathbf{k}'-\mathbf{G}} \rangle, \quad (7)$$

where λ is the form factor for the non-interacting continuum band. This can be approximately rewritten in the

renormalized band basis as,

$$\begin{aligned} E_{Fock} &\approx - \sum_{\mathbf{k}, \mathbf{k}' \in BZ} V_{\mathbf{k}-\mathbf{k}'} |\tilde{\lambda}_{\mathbf{k}, \mathbf{k}'}|^2 \langle \psi_{\mathbf{k}}^\dagger \psi_{\mathbf{k}} \rangle \langle \psi_{\mathbf{k}'}^\dagger \psi_{\mathbf{k}'} \rangle \\ &= - \sum_{\mathbf{k}, \mathbf{k}' \in BZ} V_{\mathbf{k}-\mathbf{k}'} |\tilde{\lambda}_{\mathbf{k}, \mathbf{k}'}|^2, \end{aligned} \quad (8)$$

where $\tilde{\lambda}_{\mathbf{k}, \mathbf{k}'} = \sum_{\mathbf{G}} u_{\mathbf{G}}^*(\mathbf{k}) u_{\mathbf{G}}(\mathbf{k}') \lambda_{\mathbf{k}+\mathbf{G}, \mathbf{k}'+\mathbf{G}}$ is the form factor for renormalized band, and we have taken the insulator ansatz $\langle n_{\mathbf{k}} \rangle = 1$ in the lowest band. We recall that the quantum metric determines the magnitude of the form factor in the small- q density operator of the renormalized band. For small momentum separation $q = k - k' \ll G$, the magnitude of form factor decays as $|\tilde{\lambda}_{\mathbf{k}, \mathbf{k}'}|^2 \sim e^{-g_{\mu\nu} q_\mu q_\nu}$. With a large Berry curvature at the zone boundary, the corresponding quantum metric $g_{\mu\nu}$ is bound to be large near the zone boundary, resulting in the exponential suppression of the magnitude of Fock energy. Since the Fock energy is negative, this suggests the Fock energy is larger for an insulator with strong Berry curvature peaks.

In summary, the band folding generated by interaction tends to avoid singular structures in the quantum geometry. Therefore the Chern number is likely to be $\gamma_{BZ}/2\pi$ rounded to its nearest integer.

As discussed in the previous section, it is also essential to understand the intermediate twist angle regime, where the Hartree term is needed to stabilize the AHC. This is also the regime where currently experimental observations of IQAH are made. Firstly, from topological band theory, it is understood^{28,29} that the Chern number is determined by the symmetry indices at the invariant momentum under the point group, which is C_3 for (realistic) R5G graphene. The real question we face is how the interaction selects the particular set of symmetry indices. In the following, we formulate a theory by establishing connections between the symmetry indices at the high-symmetry momenta and the density profile of the corresponding Bloch functions.

To begin with, the eigenstate for the mean-field Hamiltonian at the \mathbf{K}_M point is

$$\psi_{\mathbf{K}_M}(\mathbf{r}) = \sum_{i=1,2,3} \alpha_i \psi_{\mathbf{K}_i}(\mathbf{r}) \quad (9)$$

where \mathbf{K}_M is the moiré K point measured from the graphene Dirac point K_D corresponding to valley +, and K_i 's are the three equivalent moiré K points. The 10-component wavefunction $\psi_{\mathbf{k}}(\mathbf{r}) = e^{i(\mathbf{k}+\mathbf{K}_D)\cdot\mathbf{r}} u_{\mathbf{k}}^0(\mathbf{r})$ is the plane wave corresponding to the lowest conduction band (denoted by 0) of the continuum model. Expressed in the 10-orbital basis described in Sec. II, the periodic Bloch function is $u_{\mathbf{k}}^0(\mathbf{r}) = (u_{A_1\mathbf{k}}, u_{B_1\mathbf{k}}, u_{A_2\mathbf{k}}, u_{B_2\mathbf{k}}, u_{A_3\mathbf{k}}, u_{B_3\mathbf{k}}, u_{A_4\mathbf{k}}, u_{B_4\mathbf{k}}, u_{A_5\mathbf{k}}, u_{B_5\mathbf{k}})^T$. Alternatively, one can express the Bloch function u^0 in real space, instead of the 10-orbital basis,

$$u_{\mathbf{k}}^0(\mathbf{r}) = \sum_n u_{n,\mathbf{k}}^0(\mathbf{r}) = \sum_n u_n(\mathbf{k}) \delta^2(\mathbf{r} - \mathbf{r}_n - \mathbf{R}), \quad (10)$$

where \mathbf{r} is a 3-dimensional position vector, \mathbf{R} labels the R5G unit cell, and \mathbf{r}_n is the displacement of the n^{th} of the orbital (in the 10-orbital basis) within the R5G unit cell.

The prominent C_3 axis is defined to run through a B_5 site at $r = 0$, and its corresponding operation is,

$$\mathbf{r} \rightarrow C_3 \circ \mathbf{r}. \quad (11)$$

This operation transforms $\psi_{\mathbf{K}_M}(\mathbf{r})$ into

$$C_3 \circ \psi_{\mathbf{K}_M}(\mathbf{r}) = \psi_{\mathbf{K}_M}(C_3 \circ \mathbf{r}) = \sum_{i=1,2,3} \alpha_i \psi_{\mathbf{K}_i}(C_3 \circ \mathbf{r}). \quad (12)$$

We note that there is a gauge degree of freedom $\psi_{\mathbf{k}} \rightarrow \psi_{\mathbf{k}} e^{i\theta_{\mathbf{k}}}$. To fix a gauge, we demand that the plane wave solution for the continuum model preserves C_3 , explicitly

$$\psi_{\mathbf{k}}(C_3 \circ \mathbf{r}) = \psi_{C_3^{-1} \circ \mathbf{k}}(\mathbf{r}), \quad (13)$$

so that there is no ambiguity for $\mathbf{k} = \mathbf{\Gamma}$. With this gauge choice, from Eq. 12 we immediately get

$$C_3 \circ \psi_{\mathbf{K}_M}(\mathbf{r}) = \sum_{i=1,2,3} \alpha_i \psi_{\mathbf{K}_i}(C_3 \circ \mathbf{r}) = \sum_{i=1,2,3} \alpha_{i+1} \psi_{\mathbf{K}_i}(\mathbf{r}) \quad (14)$$

where we have made the convention $\mathbf{K}_{i+1} = C_3 \circ \mathbf{K}_i$. The conclusion from Eq. 14 is striking: the C_3 operation cyclically permutes the coefficients $(\alpha_1, \alpha_2, \alpha_3)$. The C_3 permutation has an eigenvalue of $-1, 0, 1$.

The eigenvalues of the C_3 operation provide the location of the peak of the Bloch function (of \mathbf{K}_M) in the moiré unit cell. For this purpose, we separate out the fastly-varying momentum K_D from the global phase,

$$\psi_{\mathbf{K}_M} = \sum_i \alpha_i \psi_{\mathbf{K}_i}(\mathbf{r}) = e^{i\mathbf{K}_D \cdot \mathbf{r}} \sum_i \alpha_i e^{i\mathbf{K}_i \cdot \mathbf{r}} u_{\mathbf{K}_i}^0(\mathbf{r}), \quad (15)$$

to obtain the amplitude on orbital n ,

$$|\psi_{\mathbf{K}_M}^n(\mathbf{r})| = \left| \sum_i \alpha_i e^{i\mathbf{K}_i \cdot \mathbf{r}} u_{n\mathbf{K}_i} \right|. \quad (16)$$

From the gauge choice of Eq. 13, the C_3 transformation on the periodic part of the Bloch function ($u_{n\mathbf{K}_i}$ for $i = 1, 2, 3$) generates a relative phase,

$$\begin{aligned} C_3 \circ \psi_{\mathbf{K}_i}(\mathbf{r}) &= e^{i(\mathbf{K}_i + \mathbf{K}_D) \cdot (C_3 \circ \mathbf{r})} u_{\mathbf{K}_i}^0(C_3 \circ \mathbf{r}) \\ &= e^{iC_3^{-1} \circ (\mathbf{K}_i + \mathbf{K}_D) \cdot \mathbf{r}} u_{\mathbf{K}_i}^0(C_3 \circ \mathbf{r}) \\ &= e^{i(\mathbf{K}_{i-1} + \mathbf{K}_D) \cdot \mathbf{r}} (e^{i\mathbf{G}_g \cdot \mathbf{r}} u_{\mathbf{K}_i}^0(\mathbf{r})) \end{aligned} \quad (17)$$

$$\begin{aligned} &\equiv \psi_{C_3^{-1} \circ \mathbf{K}_i}(\mathbf{r}) \\ &= e^{i(\mathbf{K}_{i-1} + \mathbf{K}_D) \cdot \mathbf{r}} u_{\mathbf{K}_{i-1}}^0(\mathbf{r}). \end{aligned} \quad (18)$$

To obtain Eq. 17, we have used the periodic nature of $u_{\mathbf{K}_i}^0(\mathbf{r})$, and $C_3 \circ \mathbf{r} = \mathbf{r} \pmod{\mathbf{R}}$, and $C_3^{-1} \circ \mathbf{K}_D = \mathbf{K}_D + \mathbf{G}_g$, where \mathbf{G}_g is a reciprocal lattice vector for the

graphene lattice. Then it becomes clear that the bracketed term in Eq. 17 is,

$$\begin{aligned} e^{i\mathbf{G}_g \cdot \mathbf{r}} u_{\mathbf{K}_i}^0(\mathbf{r}) &= e^{i\mathbf{G}_g \cdot \mathbf{r}} \sum_{n, \mathbf{R}} u_{n\mathbf{K}_i} \delta^2(\mathbf{r} - \mathbf{r}_n - \mathbf{R}) \\ &= \sum_{n, \mathbf{R}} e^{i\mathbf{G}_g \cdot \mathbf{r}_n} u_{n\mathbf{K}_i} \delta^2(\mathbf{r} - \mathbf{r}_n - \mathbf{R}), \end{aligned} \quad (19)$$

where we employ the delta-function constraint. Comparing Eq. 17 with 18, and combining with Eq. 19, we find the relation between the 10-component Bloch state vector $u_{n\mathbf{k}}$ to its C_3 transformed counterpart ($u_{n(C_3 \circ \mathbf{k})}$),

$$u_{n(C_3 \circ \mathbf{k})} = S_{nn} u_{n\mathbf{k}} \quad (20)$$

where S is a diagonal matrix $S = e^{-i\mathbf{G}_g \cdot \mathbf{r}_n} = \text{diag}(\omega^2, \omega^1, \omega^1, 1, 1, \omega^2, \omega^2, \omega^1, \omega^1, 1)$, with $\omega = e^{i2\pi/3}$. This leads to,

$$u_{n\mathbf{K}_{i+1}} = S_{nn} u_{n\mathbf{K}_i}. \quad (21)$$

Thus, for a Bloch state with C_3 symmetry index L , we have the corresponding eigenvalues $\alpha = (1, \omega^L, \omega^{2L})$. The corresponding amplitude is,

$$\rho_{\mathbf{K}_M}^n(r) = |\psi_{\mathbf{K}_M}^n(\mathbf{r})|^2 \sim \left| \sum_{j=1,2,3} \omega^{jL} S_{nn}^j e^{i\mathbf{K}_j \cdot \mathbf{r}} \right| |u_{n\mathbf{K}_1}|^2. \quad (22)$$

The peak location is where the three plane waves constructively interfere.

For example, for a state with C_3 index $L = 0$, the density profile on orbital B_5 (meaning $S_{nn} = 1$) peaks at origin $\mathbf{r} = 0$, while for $L = 1$, the peak of B_5 density shifts to a corner of the hexagonal moiré unit cell \mathbf{r}_1 , which satisfies $e^{i\mathbf{K}_j \cdot \mathbf{r}_1} = \omega^{-j}$, so that the j -dependent phase e^{jL} gets canceled at \mathbf{r}_1 . Similarly, the peak of density for orbital B_5 and B_4 are located at different high symmetry locations in the hexagonal moiré unit cell (see Fig. 4)

Finally, note that \mathbf{K}_M and $\bar{\mathbf{K}}_M$ are connected through a C_2 rotation. As their symmetry indices interpolate from $L = 0$ to $L = 1$, the peaks for $\rho_{\mathbf{K}_M}^n(r)$ and $\rho_{\bar{\mathbf{K}}_M}^n(r)$ get shifted from the origin to opposite corners of the hexagonal moiré unit cell. As a result, non-trivial C_3 indices at \mathbf{K}_M and $\bar{\mathbf{K}}_M$ would reduce the Hartree energy between these two Bloch states, due to minimizing the wavefunction overlap. This is why the Hartree term selects the set of symmetry indices to be $(L_\Gamma, L_{\mathbf{K}}, L_{\bar{\mathbf{K}}}) = (0, 1, 1)$, which gives $C = -1$.

We demonstrate the effects of the spatial separation of the Bloch functions explicitly by considering the effects of Hartree and Fock terms. In Fig. 3, we show the phase diagram with only the Fock term, and with both Hartree and Fock terms. In the range of twist angles close to experimental regime $0.6^\circ < \theta < 0.9^\circ$, the Fock term opens an energy gap, but it is the Hartree term that selects a $C = -1$ state. It is important to note that our above arguments are valid in this relatively small range

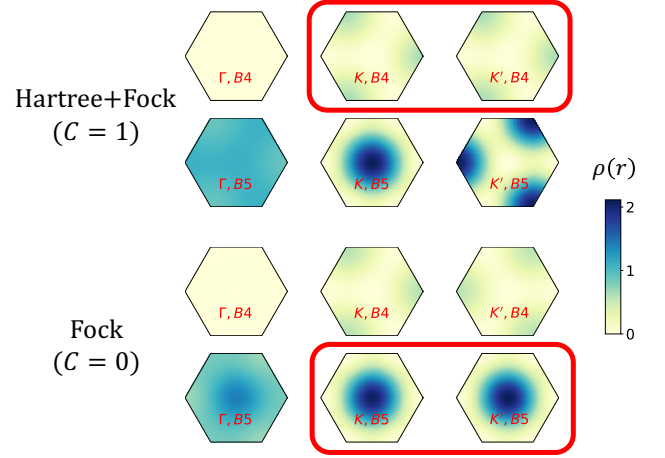


Figure 4. Real-space B_4 and B_5 density profile for Bloch functions at high symmetry momentum. With the Hartree term included, the B_5 orbitals repel and the density profile is spread out to different regions of the moiré unit cell, while the B_4 orbitals overlap. Without the Hartree term, the Fock energy is reduced by overlapping B_5 orbitals. These results are obtained for $\theta = 0.7^\circ$, $u_d = -30\text{meV}$, and with a very weak moire potential $C_{AA} = C_{BB} = 1\text{meV}$ to pin the wavefunction to high symmetry positions in the unit cell.

of twist angle. When θ becomes very large, the first BZ is no longer completely within the flat region. Therefore at BZ boundaries, the Bloch function no longer has its weight concentrated on B_4 and B_5 orbitals. Nonetheless, the $C = -1$ state in this regime can still be understood from the γ_{BZ} of the non-interacting band, as described in Sec. III. On the other hand, when θ becomes very small, the Bloch functions near the center of BZ retain strongly non-uniform density profiles in real space, since $c_{\mathbf{k}}$ and $c_{\mathbf{k}+\mathbf{G}}$ are not far away in energy and can hybridize strongly. In this case, it is no longer justified to consider the subsystem of only K and \bar{K} points.

V. SIMPLIFIED MODEL FOR COMPETING INSULATORS BASED ON PSEUDOPOTENTIAL AT MBZ CORNERS

In this part, we reformulate the story in the Sec. IV in a more elegant way, in the spirit of a Landau theory. We will focus on the interplay between Bloch states at MBZ corners \mathbf{K}_M and $\bar{\mathbf{K}}_M$, and show explicitly how the C_3 eigenvalues at these two high-symmetry points are chosen to be non-trivial by the Coulomb interaction.

For any insulating state, the filling is $n_k = 1$ at both \mathbf{K}_M and $\bar{\mathbf{K}}_M$ points. Therefore, at the mean-field level and assuming a C_3 -preserving ansatz, the low-energy degrees of freedom describing the competition between AHC and WC are two angular variables (classical rotors), θ_1 and θ_2 , associated with the two MBZ corners \mathbf{K}_M and $\bar{\mathbf{K}}_M$. Each rotor variable may take value from $\{0, 2\pi/3, 4\pi/3\}$, corresponding to C_3 symmetry index of

0, 1, and 2. Note that, in our setting, the Γ point of the MBZ which obviously is also C_3 symmetric has a trivial C_3 index. Thus it is sufficient to focus on the two MBZ corners K_M and \bar{K}_M .

Here we would like to add two remarks: (1) Although C_3 indices are only well-defined at the high-symmetry points K_M and \bar{K}_M , their values also determine the surrounding measure-nonzero regions since the Bloch function is continuous in k -space. Therefore, it is conceivable that these indices may be associated with the energy of many-body state. (2) Although the C_3 indices cannot directly be thought of as order parameters since they are not associated with symmetry breaking, they carry sufficient information to distinguish the WC and AHC phases. Therefore, as we focus on the competition between the two phases, we can still follow the spirit of Landau, by treating C_3 indices $\theta_{1,2}$ as the relevant ‘‘macroscopic’’ variables for our simplified model, and then study how the symmetry of the system constrains the ground state energy as a function of $\theta_{1,2}$.

Note that the C_3 index is defined modulo 3. The angular nature of $\theta_{1,2}$ demands that the ground state energy be invariant under $\theta_1 \rightarrow \theta_1 + 2n\pi$, $\theta_2 \rightarrow \theta_2 + 2m\pi$, which constrains the effective model to be of the form of a 2-site and 3-state classical Potts model,

$$H_{\text{eff}} = -J_+ \cos(\theta_1 + \theta_2 - \phi_+) - J_- \cos(\theta_1 - \theta_2 - \phi_-) + h_1 \cos(\theta_1 - \phi_1) + h_2 \cos(\theta_2 - \phi_2). \quad (23)$$

In the absence of moiré potential, the Hamiltonian is further constrained by a translational symmetry that translates the center of the hexagonal moiré unit cell to its corner (see Fig. 8). This translation alters the C_3 indices at two MBZ corners in opposite directions, namely, $\theta_1 \rightarrow \theta_1 + 2\pi/3$, $\theta_2 \rightarrow \theta_2 - 2\pi/3$. The proof is detailed in Appendix B. Therefore, the only term allowed by symmetry is

$$H_{\text{eff}} = -J \cos(\theta_1 + \theta_2 - \phi) \quad (24)$$

We note that in more generic settings, where all high symmetry momenta are ‘‘activated’’ (meaning hybridization between \mathbf{k} and $\mathbf{k} + \mathbf{G}$ is strong), the model should involve three sites, which may have richer physics due to frustration. But in this work, we will stick to this simple and experimentally relevant two-site model. We emphasize again that the simplified model Eq. 24 is different from the standard Landau framework. This is not a theory for low energy fluctuations; rather it only captures the competition between the 9 local minima of energy topography, which appear when C_3 symmetry is enforced. In the usual Landau framework, high-energy fluctuations are integrated out to generate a low-energy effective Landau energy function. Here, in the same spirit, we find energy minimum in the space of the C_3 indices.

As we show in detail in Appendix C, the parameters J and ϕ can be extracted from the microscopic interacting Hamiltonian at the mean-field level. This procedure is essentially rewriting the interaction in terms of

pseudopotential in angular momentum channels for the MBZ corners. The effective simplified model contains both Hartree and Fock terms. In the twist angle range around $\theta \approx 0.77$ and the limit of the electronic density predominantly on the B_5 orbital (noted in Ref. 12), we analytically show that the Hartree term dominates and selects the $|C| = 1$ state as the ground state, in agreement with the conclusion in Sec. IV.

VI. COMPETING FERMI LIQUID AND HALL CRYSTAL PHASES

In the absence of the moiré potential, a natural candidate for the ground state (in addition to the aforementioned Wigner/Hall crystal states) is the Fermi liquid, which preserves translational symmetry. To provide a quantitative comparison of the crystal and liquid states in the moiré-less setting, we examine their competition within the framework of Hartree-Fock theory. To that end, the Hall crystal is signified by the breaking of the translational symmetry by selecting (in momentum space) a reciprocal lattice vector \mathbf{G} . As a standard, we take the reciprocal lattice vector to correspond to that of a moiré unit cell with hBN aligned at the experimentally relevant twist angle 0.77° . In the framework of mean-field theory, this corresponds to $\langle c_{\alpha, \mathbf{k} + \mathbf{G}}^\dagger c_{\beta, \mathbf{k}} \rangle \neq 0$, where the Greek indices indicate a generalized spin/valley/band degree of freedom. The Fermi liquid, on the other hand, preserves continuous translation symmetry; this corresponds to the mean-field density matrix $\langle c_{\alpha, \mathbf{k}}^\dagger c_{\beta, \mathbf{k}} \rangle \neq 0$.

At the level of Hartree-Fock, the Fermi liquid state is found to be higher in energy than Hall crystal by $\sim 5\text{meV}$ per unit cell (see Fig. 10 in Appendix D). This may naively suggest that the moiré-less setting is partial to the formation of the electronic crystal phase. However, it is important to emphasize that the above quantitative comparison is within the framework of Hartree-Fock theory, and it is important to re-evaluate the FL-AHC competition beyond Hartree-Fock as we elaborate below.

VII. BEYOND HARTREE-FOCK: COMMENTS ON THE TRUE PHASE DIAGRAM, AND ON PHENOMENOLOGY

In jellium, Hartree-Fock theory famously severely overestimates^{30,31} the stability of the Wigner Crystal. It predicts that the WC crystal forms at an $r_s \approx 1.2 - 1.4$ ($r_s = \frac{l}{a_0}$ is the ratio of the inter-electron spacing l with the Bohr radius a_0 , and is the standard measure of the ratio of kinetic and Coulomb energies for quadratically dispersing bands). Detailed Monte Carlo calculations^{32,33}, however, show that the true transition to the WC does not occur till an $r_s^{\text{true}} \approx 30$. For large values of $r_s < r_s^{\text{true}}$, the ground state is a strongly correlated Fermi liquid. This state is stabilized relative to the WC by a very small energy³³ (about a fraction of $\mathcal{O}(10^{-3})$) over a large range

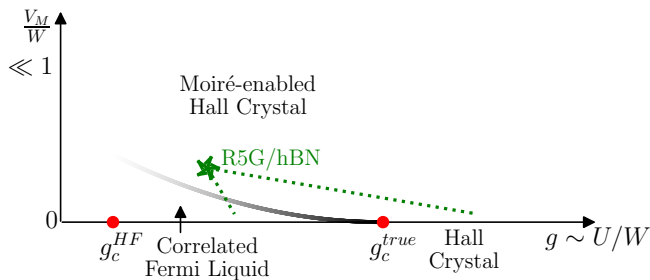


Figure 5. Schematic phase diagram showing the competition between the Fermi liquid and the Hall crystal, both at zero and non-zero moiré potential strength V_M . The parameter g is a measure of the ratio of Coulomb (U) to kinetic (W) energies. Even if the Hall crystal is not the true ground state (beyond Hartree-Fock), it can be stabilized by a weak moiré potential, a state we denote the ‘moiré-enabled Hall crystal’. A possible location of R5G/hBN is indicated by the green star at a not-too-high displacement field. The dashed green lines indicate the possible fate of the system under increasing displacement field. The evolution may either move the system into the pristine AHC phase $g > g_c^{true}$ weakly pinned by the moiré potential, or fall short and land in the FL phase with $g < g_c^{true}$.

of r_s). This tiny stabilization energy can be rationalized by noting that, at short distances and short times, the liquid behaves essentially the same as the solid and thus the two states have the same potential energy. At late times, however, the liquid can flow, and this presumably leads to a slight lowering of the kinetic energy compared to the crystal. This observation underlies a picture of the strongly correlated Fermi liquid as an ‘almost localized’ or ‘nearly frozen’ liquid^{34,35}, as appreciated a long time ago for ordinary liquids³⁶.

Moiré-enabled AHC: Returning to R5G, we expect a similar situation. Consider the phase diagram at a density where the Hall crystal is stabilized in the Hartree-Fock approximation. Let g be a dimensionless parameter that measures the ratio of Coulomb (U) and kinetic (W) energies. The Coulomb scale is $U = \frac{e^2}{\epsilon l}$ where ϵ is the dielectric constant, and l is the inter-electron spacing. The scale W for the kinetic energy can be taken to be the bandwidth within the first MBZ with the moiré potential turned off. Then we expect that the true g_c^{true} at which the transition³⁷ to the Hall crystal occurs to be (substantively) larger than the Hartree-Fock g_c^{HF} . This is depicted schematically in Fig. 5. For $g_c^{HF} < g < g_c^{true}$, we expect that the ground state is a correlated Fermi liquid that is ‘almost localized’. Further, we expect that the ground state energy per particle of the Fermi liquid is smaller by only a small amount compared to that of the Hall crystal.

We leave the precise phase diagram as an interesting target for future numerical work using, say, Variational Monte Carlo methods. For now, consider the phase diagram in the presence of a periodic moiré potential. The expected small stabilization energy of the Fermi liquid

over the Hall crystal implies that even a weak moiré potential will induce a transition from Fermi liquid to a Chern insulator. This is because the Hall crystal gains commensuration energy in the moiré potential which will overcome the small energy by which the Fermi liquid is stabilized. To see this, consider the energy (per particle) of both the Fermi liquid and the Hall crystal. We denote these $E_{FL}(g, V_M)$ and $E_{HC}(g, V_M)$ respectively. At the (first order) FL-HC transition at $V_M = 0$, we have

$$E_{FL}(V_M = 0, g_c^{true}) = E_{HC}(V_M = 0, g_c^{true}). \quad (25)$$

As g decreases slightly below g_c , we will have

$$E_{FL}(V_M = 0, g) = E_{HC}(V_M = 0, g) - a(g_c^{true} - g) + \dots \quad (26)$$

with $a > 0$, and the ellipses represent higher-order terms in $(g_c^{true} - g)$. Now let us consider the energies when a small V_M is turned on. The crystal will lower its energy at linear order in V_M :

$$E_{HC}(V_M, g) = E_{HC}(V_M = 0, g) - bV_M + \dots \quad (27)$$

where now the ellipses represent higher order terms in V_M , and $b > 0$. However the Fermi liquid will only have a change at quadratic order in V_M :

$$E_{FL}(V_M, g) = E_{FL}(V_M = 0, g) - c(V_M)^2 + \dots \quad (28)$$

with $c > 0$. Thus the Hall crystal will win over the Fermi liquid when

$$bV_M - cV_M^2 > a(g_c^{true} - g) \quad (29)$$

It follows that the phase boundary will have the shape shown in Fig. 5. (For a recent numerical study³⁸ of a similar phase competition between the FL and the ordinary WC in TMD moire materials, see Ref.³⁹). Further, we expect that even somewhat far below g_c^{true} , the critical V_M needed to stabilize the Hall crystal is small. The moiré induced FL to (pinned) Hall crystal state will be first order (at least with a screened Coulomb interaction).

We call the Chern insulating state induced by V_M a ‘moiré-enabled AHC’. This state is likely stable over a much wider range of the phase diagram than the pristine AHC which exists in the strictly translation-invariant system.

We do not of course know where R5G/hBN sits in this phase diagram, but it is conceivable that in a range of displacement fields it is in the moiré-enabled AHC regime (denoted by green star in Fig. 5). If that is the case, the moiré-less (*i.e.* unaligned R5G) will be a Fermi liquid metal (with spin/valley polarization). Aligning with hBN will, in a range of twist angles, push the system across the phase boundary to the moiré-enabled AHC. So long as the effective V_M felt by the electrons in the occupied layers is small (as is expected at the large displacement fields needed to stabilize the QAH states in R5G), the charge gap of the moiré-enabled AHC state will be determined by the strength of the Coulomb interaction, and not by the strength of the moiré potential.

Thus, even if the moiré is needed to stabilize the Chern insulator, the physics is still primarily determined by the Coulomb interactions. The sole role of the moiré potential is to tip the delicate balance of energy between the Fermi liquid and Hall crystal.

Note that increasing the displacement field has a number of different effects: it changes the ratio of kinetic and Coulomb energies and thus increases g ; it also reduces the effective V_M as the conduction electrons get driven further away from the aligned hBN side; finally, it also changes the Berry curvature distribution. Changing Berry curvature is not included in the schematic phase diagram Fig. 5; we have already discussed its role in determining the selection between the AHC and the ordinary WC. In the context of Fig. 5, increasing $|u_d|$ thus corresponds to both increasing g and decreasing V_M , which thus pushes the system closer to the pristine AHC, but may also take it back to the FL.

Doping away from commensuration: It is also very interesting to ask what happens at densities that are not commensurate with the moiré potential, assuming we are at $g < g_c^{true}$. For instance, consider decreasing the density so that if any crystal forms it will have a larger lattice spacing than the moiré potential. If the density deviation from the commensurate value is small, we may expect that the crystal pays the cost of the extra elastic energy to lock its period to the moiré lattice so as to gain commensuration energy. The density deficit will then be accommodated by a non-zero density of vacancies (equivalent, in a weak coupling picture, to ‘doping the Chern band’). Such a state may still overcome the Fermi liquid if the commensuration energy is big enough. These vacancies (i.e the doped holes) can then form FQAH states at the suitable fillings. Alternately, if g is not close enough to g_c^{true} , the Fermi liquid may win out at the lower density and the system forms a metallic state. The locking to the moiré potential becomes less likely the lower the density is. Thus at low densities (well below $\nu = 1$) the primary competition will be between the Fermi liquid and a crystal (either AHC or WC) that has its natural intrinsic period. However, from the Hartree-Fock calculations, we also know that at low density (*i.e* low θ), the WC is favored over the AHC as the Berry curvature in the first MBZ of the non-interacting band is small. Thus at densities well below $\nu = 1$, the two main players will be the Fermi liquid and the WC with the latter winning at the lowest densities. These expectations are qualitatively consistent with the phase diagram reported in Ref. 11.

A more radical possibility is that of a fractional AHC, where even for $g > g_c^{true}$ and in the absence of moiré, the system prefers to lock in a specific density and accommodate any density deficit through vacancies that form an FQAH state. While we are not aware of a strong reason forbidding such a state to exist, it is likely not stable energetically at densities so low that half the lattice is empty. Thus, this possibility may not be supported in the current experiments where FQAH states are seen down to

filling $\nu = 2/5$; however it is an interesting possibility that could be relevant as more RnG systems are studied.

Disorder effects: Finally, we briefly discuss what we might expect in moiré-less R5G in the presence of weak disorder. If the ground state in the clean limit is an AHC, then it will be randomly pinned by the impurities (and long-range crystalline order will be lost). The resulting state will be a disordered IQAH insulator. If $g < g_c^{true}$, and the ground state is a correlated Fermi liquid, then locally near each impurity, we might expect, for the same reason as above, that the delicate balance between FL and AHC is tipped in favor of the AHC beyond a non-zero but small value. Thus we expect puddles of randomly oriented AHC to nucleate within the metallic state (ignoring Anderson localization effects which will not set in up to parametrically larger scales for weak disorder). At stronger disorder strength, there will be a transition to the disordered IQAH insulator.

In transport experiments, the sliding motion of the ideal, clean AHC will lead to an infinite longitudinal conductivity, and a finite Hall conductivity (so that the Hall resistivity is zero). Once the AHC is pinned, either by a periodic potential, or by disorder, the DC longitudinal conductivity at low bias voltage will be zero while the Hall conductivity will be quantized, exactly as expected of an IQAH insulator. In the clean Fermi liquid metallic state, with very weak disorder, the Berry curvature enclosed within the Fermi surface (Φ_B) will lead to an anomalous Hall conductivity $\sigma_{xy}^{FL} = \frac{e^2}{h} \frac{\Phi_B}{2\pi}$ but this will be much smaller than the longitudinal conductivity $\sigma_{xx}^{FL} = \frac{e^2}{h} (K_F l_{mf})$ (K_F is the Fermi momentum and l_{mf} is the mean free path) so that the Hall resistivity will be small. As the disorder increases, there will be the puddles of AHC nucleated by the disorder, which will presumably lead to an enhanced, but not quantized, Hall resistivity.

VIII. ROUTES TO HIGHER CHERN BANDS IN ELECTRON-DOPED RnG

The discussion of the interaction-induced Chern band/AHC in RnG has primarily focused on fully/partially filling a $|C| = 1$ band¹²⁻¹⁴. In this section, we examine the possibility of finding (within Hartree-Fock) similar interaction-induced IQAH states with $|C| > 1$ for electron-doped RnG. We explore two routes where such a $|C| > 1$ state may occur. In the calculations below, we have included the warping terms that have been ignored so far.

Firstly, we consider the Hartree-Fock phase diagram in R5G/hBN as a function of the twist angle (θ) and the strength V_m of the moiré potential. Though naively the microscopic moiré potential is fixed by the alignment to the hBN, there is uncertainty on details like the lattice relaxation that may modify it. Thus we simply take the overall magnitude of V_M as a tuning parameter to illustrate the possibilities. We present in Fig. 6 the HF-phase diagram for these moiré tuning parameters, where

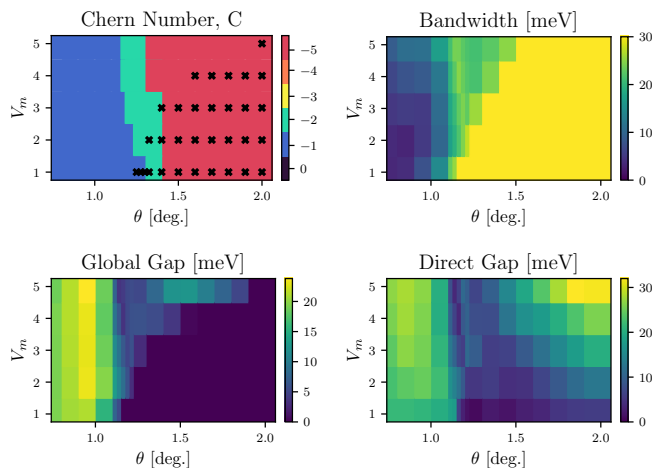


Figure 6. Hartree-Fock bands indicating Chern number and bandwidth of the active band, global band gap, and direct band gap to nearest conduction band for twist angles (θ) and moiré potential strengths (V_m) of the full 10-orbital model (including all warping terms). The displacement field energy is $u_d = -36$ meV, and the dielectric constant is $\epsilon = 8$. The Chern number is well-defined when the direct band gap is non-zero (≥ 0.5 meV). The ‘crossed’ out yellow boxes in the Chern number indicate cases where the global bandgap is zero (< 0.5 meV), while the direct band gap is still non-zero (i.e. there is an indirect band gap – the system is metallic). Phase diagrams are for a mesh of 21×21 , with 4 conduction bands in total (1 active band and 3 remote bands above), and constructed using 19 moiré Brillouin zones, and generated using at least six distinct initial mean-field ansatzes for a given parameter point.

we depict the Chern number, bandwidth, and gaps of the active band. As seen, for the naive moiré strength, the $|C| = 1$ state is the only state that is well isolated; the ‘crossed’ out yellow boxes in the Chern number indicate cases where the global bandgap is zero (< 0.5 meV), while the direct band gap is still non-zero (i.e. there is an indirect band gap and the system is metallic). However, with an enhanced moiré potential to open up the band gap, we can obtain high Chern number bands that are well isolated. In these regions, the mean-field bandwidth is ~ 20 meV, with a direct gap of $\sim 5 - 10$ meV (and a global gap of $3 - 6$ meV). In particular, topologically non-trivial bands of $|C| = \{2, 5\}$ are formed.

Secondly, we examine the regime of strong interactions (enabled by imagining decreasing the dielectric constant ϵ) without warping terms. We present in Fig. 7 the possible Chern numbers as a function of twist angle and displacement field energy for enhanced electron-electron interactions. Once again, in addition to $|C| = 1$ state, higher Chern bands are found to develop, for increasing twist angles.

These routes that lead to bands with enhanced Chern number provides the intriguing possibility to realize incompressible states by fully/partially filling these higher-Chern bands. We hope that these results provide enough

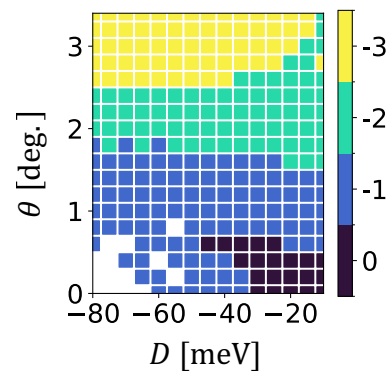


Figure 7. Phase diagrams in $\theta - u_d$ space indicating the Chern number, obtained with the same non-interacting parameters as in Fig. 3, but with an enhanced interaction $\epsilon = 2$ (as compared to $\epsilon = 6$). This result is obtained for the simplified model without warping terms. We use a momentum mesh of 18×18 , and include 4 conduction bands.

motivation for future experimental studies of the higher twist angle region, and more detailed theoretical modeling.

IX. DISCUSSION

In this work, we examined the origins of the interaction-induced IQAH in R5G/hBN, and the closely related AHC in moiré-less R5G. Focussing on an effective continuum model of R5G, we trace the origin of $|C| = 1$ band to the appreciable flux contained about the zone center and the crucial but differing roles played by the Hartree and Fock interaction terms. At a slightly larger alignment angle (or equivalently charge densities corresponding to lattice filling $\nu = 1$) than in current experiments, the Fock term alone is enough to both open a band gap and to endow the occupied band with Chern number. At lower alignment angles, including the one in current devices, the Fock term opens the gap while the preference for the non-zero Chern number comes from the Hartree term.

We reiterate that, though the ‘dangling edge’ model of pentagraphene (effective k^5 -two-orbital model) captures the ring-like feature of the continuum Berry curvature, it importantly misses on the approximately $-\pi$ -Berry flux contained about $k = 0$, that becomes ever-increasingly important at large displacement fields.

Examination of the continuum model, in the absence of trigonal warping terms (that are included in quantitative studies of multilayer graphene) and the moiré potential, provides a remarkably intuitive understanding of the Hartree-Fock results. For large ($0.9^\circ < \theta < 1.5^\circ$) twist angles, where the MBZ boundary intersects the Berry-curvature ring, the MBZ contains appreciable Berry flux (between π and 3π), leading the Fock term to merely introduce band gaps and shunting the subsequent flux

to the closest integer. At the intermediate twist angle regime, relevant for the existing experiments¹¹, the importance of the Hartree interaction in developing a $|C| = 1$ band is understood heuristically in terms of the topologically non-trivial band possessing more spread-out charge distribution. Our simplified model provides a quantitative justification for this conclusion.

The ultimate fate of the non-moiré and the moiré R5G relies on the competition of correlated Fermi liquid, Wigner crystal, and anomalous Hall crystal states. In addition to Hartree-Fock estimates of the energy differences, we discussed simple expectations for what may happen beyond Hartree-Fock. Specifically, even if a correlated FL, rather than the AHC, is the true ground state in moiré-less RnG, even a very weak moiré potential can tip the Hall crystal to be lower in energy over the Fermi liquid state. This is because we anticipate that, in the moiré-less setting (by analogy with the usual two-dimensional electron fluid), the FL and AHC will likely have very similar ground state energy, and the AHC can gain commensuration energy from the periodic potential. This simple observation allows us to envision the possibility that such a moiré-enabled AHC (if not the pristine AHC itself) occupies a wide region of the phase diagram (at the fixed density corresponding to $\nu = 1$, as a function of interaction strength and moiré potential strength), even beyond Hartree-Fock. It is clearly important to study these questions with robust numerical methods (such as Variational Monte Carlo) in the future.

Finally, by exploring the phase diagram at slightly larger alignment angles than in current devices, we sug-

gest that it may be possible to stabilize interaction-induced higher Chern bands/AHCs in electron-doped RnG, which too will be interesting to study further in the future.

While this paper was being written, two interesting papers that overlap with ours - Ref. 40 and 41 - appeared. Ref. 40 studies a toy model with constant Berry curvature where the Fock term alone stabilizes an AHC. Ref. 41 considers the specific setting appropriate to RnG, and introduces a hot-spot model for the MBZ corners to discuss the stability of the AHC with some rough similarity to our discussion.

ACKNOWLEDGMENTS

We thank Ray Ashoori, Ilya Esterlis, Tonghang Han, Long Ju, Kyung-su Kim, Zhengguang Lu, Tomo Soejima, Ashvin Vishwanath, and particularly Boran Zhou and Ya-Hui Zhang for many inspiring discussions. TS was supported by NSF grant DMR-2206305, and partially through a Simons Investigator Award from the Simons Foundation. This work was also partly supported by the Simons Collaboration on Ultra-Quantum Matter, which is a grant from the Simons Foundation (Grant No. 651446, T.S.). The authors acknowledge the MIT SuperCloud and Lincoln Laboratory Supercomputing Center for providing HPC resources that have contributed to the research results reported within this manuscript.

-
- ¹ G. Chen, A. L. Sharpe, E. J. Fox, Y.-H. Zhang, S. Wang, L. Jiang, B. Lyu, H. Li, K. Watanabe, T. Taniguchi, *et al.*, *Nature* **579**, 56 (2020).
- ² M. Serlin, C. Tschirhart, H. Polshyn, Y. Zhang, J. Zhu, K. Watanabe, T. Taniguchi, L. Balents, and A. Young, *Science* **367**, 900 (2020).
- ³ S. Chen, M. He, Y.-H. Zhang, V. Hsieh, Z. Fei, K. Watanabe, T. Taniguchi, D. H. Cobden, X. Xu, C. R. Dean, *et al.*, *Nature Physics* **17**, 374 (2021).
- ⁴ H. Polshyn, J. Zhu, M. Kumar, Y. Zhang, F. Yang, C. Tschirhart, M. Serlin, K. Watanabe, T. Taniguchi, A. MacDonald, *et al.*, *Nature* **588**, 66 (2020).
- ⁵ T. Li, S. Jiang, B. Shen, Y. Zhang, L. Li, Z. Tao, T. Devakul, K. Watanabe, T. Taniguchi, L. Fu, *et al.*, *Nature* **600**, 641 (2021).
- ⁶ B. A. Foutty, C. R. Kometter, T. Devakul, A. P. Reddy, K. Watanabe, T. Taniguchi, L. Fu, and B. E. Feldman, arXiv preprint arXiv:2304.09808 (2023).
- ⁷ Y.-H. Zhang, D. Mao, Y. Cao, P. Jarillo-Herrero, and T. Senthil, *Physical Review B* **99**, 075127 (2019).
- ⁸ N. Bultinck, S. Chatterjee, and M. P. Zaletel, *Physical review letters* **124**, 166601 (2020).
- ⁹ Y.-H. Zhang, D. Mao, and T. Senthil, *Physical Review Research* **1**, 033126 (2019).
- ¹⁰ C. Repellin, Z. Dong, Y.-H. Zhang, and T. Senthil, *Physical Review Letters* **124**, 187601 (2020).
- ¹¹ Z. Lu, T. Han, Y. Yao, A. P. Reddy, J. Yang, J. Seo, K. Watanabe, T. Taniguchi, L. Fu, and L. Ju, arXiv preprint arXiv:2309.17436 (2023).
- ¹² Z. Dong, A. S. Patri, and T. Senthil, arXiv preprint arXiv:2311.03445 (2023).
- ¹³ B. Zhou, H. Yang, and Y.-H. Zhang, arXiv preprint arXiv:2311.04217 (2023).
- ¹⁴ J. Dong, T. Wang, T. Wang, T. Soejima, M. P. Zaletel, A. Vishwanath, and D. E. Parker, arXiv preprint arXiv:2311.05568 (2023).
- ¹⁵ Z. Guo, X. Lu, B. Xie, and J. Liu, arXiv preprint arXiv:2311.14368 (2023).
- ¹⁶ Y. H. Kwan, J. Yu, J. Herzog-Arbeitman, D. K. Efetov, N. Regnault, and B. A. Bernevig, arXiv preprint arXiv:2312.11617 (2023).
- ¹⁷ J. Cai, E. Anderson, C. Wang, X. Zhang, X. Liu, W. Holtzmann, Y. Zhang, F. Fan, T. Taniguchi, K. Watanabe, Y. Ran, T. Cao, L. Fu, D. Xiao, W. Yao, and X. Xu, *Nature* (2023), [10.1038/s41586-023-06289-w](https://doi.org/10.1038/s41586-023-06289-w).
- ¹⁸ Y. Zeng, Z. Xia, K. Kang, J. Zhu, P. Knüppel, C. Vaswani, K. Watanabe, T. Taniguchi, K. F. Mak, and J. Shan, *Nature* (2023), [10.1038/s41586-023-06452-3](https://doi.org/10.1038/s41586-023-06452-3).
- ¹⁹ H. Park, J. Cai, E. Anderson, Y. Zhang, J. Zhu, X. Liu, C. Wang, W. Holtzmann, C. Hu, Z. Liu, T. Taniguchi, K. Watanabe, J.-h. Chu, T. Cao, L. Fu, W. Yao, C.-Z. Chang, D. Cobden, D. Xiao, and X. Xu, *Nature* (2023),

- 10.1038/s41586-023-06536-0.
- ²⁰ F. Xu, Z. Sun, T. Jia, C. Liu, C. Xu, C. Li, Y. Gu, K. Watanabe, T. Taniguchi, B. Tong, J. Jia, Z. Shi, S. Jiang, Y. Zhang, X. Liu, and T. Li, *Phys. Rev. X* **13**, 031037 (2023).
- ²¹ Z. Tesanovic, F. Axel, and B. Halperin, *Physical Review B* **39**, 8525 (1989).
- ²² T. Han, Z. Lu, Y. Yao, J. Yang, J. Seo, C. Yoon, K. Watanabe, T. Taniguchi, L. Fu, F. Zhang, *et al.*, arXiv preprint arXiv:2310.17483 (2023).
- ²³ F. Zhang, B. Sahu, H. Min, and A. H. MacDonald, *Phys. Rev. B* **82**, 035409 (2010).
- ²⁴ C.-H. Ho, C.-P. Chang, and M.-F. Lin, *Phys. Rev. B* **93**, 075437 (2016).
- ²⁵ B. L. Chittari, G. Chen, Y. Zhang, F. Wang, and J. Jung, *Phys. Rev. Lett.* **122**, 016401 (2019).
- ²⁶ In the following discussion, we make the simplification of ignoring other on-site potentials present in the real system; they are easily incorporated when more precision is needed.
- ²⁷ The methodology of the Hartree-Fock calculations follow those in Ref. 12.
- ²⁸ T. L. Hughes, E. Prodan, and B. A. Bernevig, *Phys. Rev. B* **83**, 245132 (2011).
- ²⁹ C. Fang, M. J. Gilbert, and B. A. Bernevig, *Phys. Rev. B* **86**, 115112 (2012).
- ³⁰ J. Trail, M. Towler, and R. Needs, *Physical Review B* **68**, 045107 (2003).
- ³¹ B. Bernu, F. Delyon, M. Holzmann, and L. Baguet, *Physical Review B* **84**, 115115 (2011).
- ³² B. Tanatar and D. M. Ceperley, *Physical Review B* **39**, 5005 (1989).
- ³³ N. Drummond and R. Needs, *Physical review letters* **102**, 126402 (2009).
- ³⁴ D. Vollhardt, *Reviews of modern physics* **56**, 99 (1984).
- ³⁵ B. Castaing and P. Nozières, *Journal de Physique* **40**, 257 (1979).
- ³⁶ Y. I. Frenkel, *Kinetic Theory of Liquids* (Oxford University Press, 1946).
- ³⁷ In principle, just like in discussions of jellium (see Ref. 42 for a recent discussion), intermediate phases between the Fermi liquid and crystal may appear, particularly with unscreened long-ranged Coulomb interactions⁴³ but do not affect the essential point we make below.
- ³⁸ We thank Ilya Esterlis for discussions on this paper and related questions.
- ³⁹ Y. Yang, M. Morales, and S. Zhang, arXiv preprint arXiv:2306.14954 (2023).
- ⁴⁰ T. Tan and T. Devakul, “Parent berry curvature and the ideal anomalous hall crystal,” (2024), arXiv:2403.04196 [cond-mat.mes-hall].
- ⁴¹ T. Soejima, J. Dong, T. Wang, T. Wang, M. P. Zaletel, A. Vishwanath, and D. E. Parker, “Anomalous hall crystals in rhombohedral multilayer graphene ii: General mechanism and a minimal model,” (2024), arXiv:2403.05522 [cond-mat.str-el].
- ⁴² K.-S. Kim, I. Esterlis, C. Murthy, and S. A. Kivelson, arXiv preprint arXiv:2309.13121 (2023).
- ⁴³ B. Spivak and S. A. Kivelson, *Physical Review B* **70**, 155114 (2004).

Appendix A: Full-10 band tight-binding model for pentalayer graphene

For clarity, we present the full-10 band tight-binding model (for a given valley K/K' and spin \uparrow/\downarrow) for pentalayer graphene (see also Ref. 12):

$$H = \begin{pmatrix} 2u_d & v_0^\dagger & v_4^\dagger & v_3 & 0 & \frac{\gamma_2}{2} & 0 & 0 & 0 & 0 \\ v_0 & 2u_d + \delta & \gamma_1 & v_4^\dagger & 0 & 0 & 0 & 0 & 0 & 0 \\ v_4 & \gamma_1 & u_d + u_a & v_0^\dagger & v_4^\dagger & v_3 & 0 & \frac{\gamma_2}{2} & 0 & 0 \\ v_3^\dagger & v_4 & v_0 & u_d + u_a & \gamma_1 & v_4^\dagger & 0 & 0 & 0 & 0 \\ 0 & 0 & v_4 & \gamma_1 & u_a & v_0^\dagger & v_4^\dagger & v_3 & 0 & \frac{\gamma_2}{2} \\ \frac{\gamma_2}{2} & 0 & v_3^\dagger & v_4 & v_0 & u_a & \gamma_1 & v_4^\dagger & 0 & 0 \\ 0 & 0 & 0 & 0 & v_4 & \gamma_1 & -u_d + u_a & v_0^\dagger & v_4^\dagger & v_3 \\ 0 & 0 & \frac{\gamma_2}{2} & 0 & v_3^\dagger & v_4 & v_0 & -u_d + u_a & \gamma_1 & v_4^\dagger \\ 0 & 0 & 0 & 0 & 0 & 0 & v_4 & \gamma_1 & -2u_d + \delta & v_0^\dagger \\ 0 & 0 & 0 & 0 & \frac{\gamma_2}{2} & 0 & v_3^\dagger & v_4 & v_0 & -2u_d \end{pmatrix}, \quad (\text{A1})$$

where we employ the basis of $(A_1, B_1, A_2, B_2, A_3, B_3, A_4, B_4, A_5, B_5)$. We have also used the notation of $v_i = \frac{\sqrt{3}}{2}t_l(\pm k_x + ik_y)$ for the monolayer graphene form factors, where $k_{x,y}$ are small momenta expanded about the valley of interest, and the layer is denoted by l . Note that $\gamma_l \equiv \frac{\sqrt{3}}{2}t_l$. In the main text, $\gamma_{1,2,3,4}$ are referred to as ‘warping terms’, which correspond to the trigonal warping of rhombohedral graphene. We direct the reader to Ref. 12 for the model parameter values.

Appendix B: Effect of Translation on the C_3 indices

In this appendix, we explain how the translation operation transforms the C_3 indices at K_M and \bar{K}_M points. This data is useful in containing the possible terms in the simplified model for competing crystalline states (see

Appendix C). Under C_3 rotation, the wavefunction for moiré band transforms as

$$C_3 |\psi_{K_M}\rangle = \omega^l |\psi_{K_M}\rangle \quad (\text{B1})$$

$$C_3 |\psi_{\bar{K}_M}\rangle = \omega^s |\psi_{\bar{K}_M}\rangle \quad (\text{B2})$$

where l and s are the C_3 indices for K_M and \bar{K}_M . Under translation,

$$T_i |\psi_{K_M}\rangle = \omega^i |\psi_{K_M}\rangle \quad (\text{B3})$$

$$T_i |\psi_{\bar{K}_M}\rangle = \omega^{-i} |\psi_{\bar{K}_M}\rangle \quad (\text{B4})$$

where $T_{i+3} = T_i$, $C_3 T_i C_3^{-1} = T_{i+1}$, $i = 0, 1, 2$ corresponds to the three equivalent corners of the moiré unit cell (see Fig.8). Note

$$C_3 T_i = C_3 T_i C_3^{-1} C_3 = T_{i+1} C_3 \quad (\text{B5})$$

Therefore,

$$C_3(T_i |\psi_{K_M}\rangle) = T_{i+1} C_3 |\psi_{K_M}\rangle = \omega^{l+i+1} |\psi_{K_M}\rangle = \omega^{l+1} (T_i |\psi_{K_M}\rangle) \quad (\text{B6})$$

$$C_3(T_i |\psi_{\bar{K}_M}\rangle) = T_{i+1} C_3 |\psi_{\bar{K}_M}\rangle = \omega^{s-i-1} |\psi_{\bar{K}_M}\rangle = \omega^{s-1} (T_i |\psi_{\bar{K}_M}\rangle) \quad (\text{B7})$$

We have seen that the translations transform the C_3 indices at (K_M, \bar{K}_M) into

$$T_i : (l, s) \rightarrow (l + 1, s - 1) \quad (\text{B8})$$

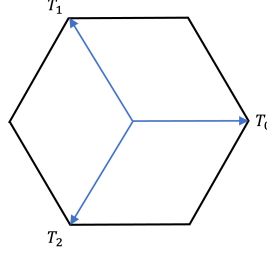


Figure 8. Definition for translation vectors.

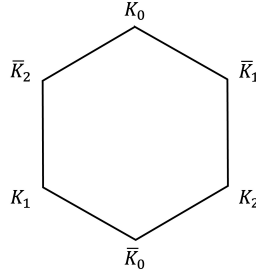


Figure 9. Labeling for MBZ corners.

Appendix C: Alternative formalism: pseudopotential in angular momentum channels

Continuing from Sec. V in the main text, in this section we detail the derivation of constants J and ϕ in the simplified model Eq. 24. To do this, we start with the interacting term of Hamiltonian projected to the lowest conduction band of the continuum model

$$H = \sum_{q,k,k'} V_q \lambda_{k,k+q} \lambda_{k',k'-q} c_k^\dagger c_{k'}^\dagger c_{k'-q} c_{k+q} \quad (\text{C1})$$

We focus on the terms within the Hilbert space of two MBZ corners K_M and \bar{K}_M . In the following, we will denote the two sets of equivalent momentum at two corners of BZ as K_i and \bar{K}_i , where $i = 0, 1, 2$ and $K_{i+1} = C_3 K_i$, $K_{n+3} = K_n$.

$$\begin{aligned}
H = & \sum_{nn'mm'} V_{K_n-K_{n'}} \lambda_{K_n, K_{n'}} \lambda_{K_m, K_{m'}} \delta^2(K_n - K_{n'} + K_m - K_{m'}) c_{K_n}^\dagger c_{K_m}^\dagger c_{K_{m'}} c_{K_{n'}} \\
& + V_{K_n-K_{n'}} \lambda_{K_n, K_{n'}} \lambda_{\bar{K}_m, \bar{K}_{m'}} \delta^2(K_n - K_{n'} + \bar{K}_m - \bar{K}_{m'}) c_{K_n}^\dagger c_{\bar{K}_m}^\dagger c_{\bar{K}_{m'}} c_{K_{n'}} \\
& + V_{K_n-\bar{K}_{n'}} \lambda_{K_n, \bar{K}_{n'}} \lambda_{\bar{K}_m, K_{m'}} \delta^2(K_n - \bar{K}_{n'} + \bar{K}_m - K_{m'}) c_{K_n}^\dagger c_{\bar{K}_m}^\dagger c_{K_{m'}} c_{\bar{K}_{n'}} \\
& + V_{K_n-\bar{K}_{n'}} \lambda_{K_n, \bar{K}_{n'}} \lambda_{K_m, \bar{K}_{m'}} \delta^2(K_n - \bar{K}_{n'} + K_m - \bar{K}_{m'}) c_{K_n}^\dagger c_{K_m}^\dagger c_{\bar{K}_{m'}} c_{\bar{K}_{n'}} \\
& + (K \leftrightarrow \bar{K}) \tag{C2}
\end{aligned}$$

$$\begin{aligned}
= & \sum_{nn'mm'} V_{K_n-K_{n'}} \lambda_{K_n, K_{n'}} \lambda_{K_m, K_{m'}} \delta_3(n - n' + m - m') c_{K_n}^\dagger c_{K_m}^\dagger c_{K_{m'}} c_{K_{n'}} \\
& + V_{K_n-K_{n'}} \lambda_{K_n, K_{n'}} \lambda_{\bar{K}_m, \bar{K}_{m'}} \delta_3(n - n' - m + m') c_{K_n}^\dagger c_{\bar{K}_m}^\dagger c_{\bar{K}_{m'}} c_{K_{n'}} \\
& - V_{K_n-\bar{K}_{n'}} \lambda_{K_n, \bar{K}_{n'}} \lambda_{\bar{K}_m, K_{m'}} \delta_3(n - n' - m + m') c_{K_n}^\dagger c_{\bar{K}_m}^\dagger c_{K_{m'}} c_{\bar{K}_{n'}} \\
& + V_{K_n-\bar{K}_{n'}} \lambda_{K_n, \bar{K}_{n'}} \lambda_{K_m, \bar{K}_{m'}} \delta_3(n + n' + m + m') c_{K_n}^\dagger c_{K_m}^\dagger c_{\bar{K}_{m'}} c_{\bar{K}_{n'}} \\
& + (K \leftrightarrow \bar{K}) \tag{C3}
\end{aligned}$$

where $\delta_3(n) = 1$ if $n \equiv 0 \pmod{3}$. Now we transform to the angular momentum basis

$$c_{l,+} = \sum_{n=0,1,2} c_{K_n} \omega^{ln} \tag{C4}$$

$$c_{l,-} = \sum_{n=0,1,2} c_{\bar{K}_n} \omega^{ln} \tag{C5}$$

where $\omega = e^{i\frac{2\pi}{3}}$. The Hamiltonian becomes

$$\begin{aligned}
H = & \sum_{ll'ss', nn'mm'} V_{K_n-K_{n'}} \lambda_{K_n, K_{n'}} \lambda_{K_m, K_{m'}} \delta_3(n - n' + m - m') \omega^{ln+sm-s'm'-l'n'} c_{l,+}^\dagger c_{l'+}^\dagger c_{s'+} c_{l'+} \\
& + V_{K_n-K_{n'}} \lambda_{K_n, K_{n'}} \lambda_{\bar{K}_m, \bar{K}_{m'}} \delta_3(n - n' - m + m') \omega^{ln+sm-s'm'-l'n'} c_{l,+}^\dagger c_{l'+}^\dagger c_{s'-} c_{l'+} \\
& - V_{K_n-\bar{K}_{n'}} \lambda_{K_n, \bar{K}_{n'}} \lambda_{\bar{K}_m, K_{m'}} \delta_3(n - n' - m + m') \omega^{ln+sm-s'm'-l'n'} c_{l,+}^\dagger c_{l'+}^\dagger c_{s'-} c_{l'+} \\
& + V_{K_n-\bar{K}_{n'}} \lambda_{K_n, \bar{K}_{n'}} \lambda_{K_m, \bar{K}_{m'}} \delta_3(n + n' + m + m') \omega^{ln+sm-s'm'-l'n'} c_{l,+}^\dagger c_{l'+}^\dagger c_{s'+} c_{l'+} \\
& + (K \leftrightarrow \bar{K}) \tag{C6}
\end{aligned}$$

To get the effective 2-site and 3-state Potts model, in the following, we will focus on the terms that conserve the fermion number in each corner. So the fourth line is dropped. The first term of Eq.C6 becomes

$$H_1 = \sum_{ls, \Delta n} V_{\Delta n} |\lambda_{\Delta n, +}|^2 \omega^{(l-s)\Delta n} c_{l,+}^\dagger c_{s,+}^\dagger c_{s,+} c_{l,+} = \sum_{ls, \Delta n, \alpha\beta} V_{\Delta n} \rho_{\alpha, +} \rho_{\beta, +} \omega^{(R_\alpha - R_\beta + l - s)\Delta n} c_{l,+}^\dagger c_{s,+}^\dagger c_{s,+} c_{l,+} \tag{C7}$$

where we have used

$$\lambda_{K_n, K_{n'}} = \langle u(K_n) | u(K_{n'}) \rangle = \sum_{\alpha} u_{\alpha}^*(K_n) u_{\alpha}(K_{n'}) = \sum_{\alpha} |u_{\alpha}(K_0)|^2 \omega^{R_{\alpha}(n-n')} = \sum_{\alpha} \rho_{\alpha, +} \omega^{R_{\alpha}(n-n')} \equiv \lambda_{n-n', +} \tag{C8}$$

here $\alpha = 0, 1, 2, \dots, 9$ labels the 10 orbitals ($B_5, A_5, B_4, A_4, \dots, B_1, A_1$), while $R_{\alpha} = (0, 1, 1, 2, 2, 3, 3, 4, 4, 5)$ is the in-plane displacement of the 10 orbitals from B_5 and

$$V_n = V(K_0 - K_n) = V(K - K \delta_{n0}) = V(K) + (V(0) - V(K)) \delta_{n0} \tag{C9}$$

As well, we have assumed that the mean-field ansatz to which this term is acted on has a conserved angular momentum (leading to $l = s$). This term does not lift the degeneracy between different angular momentum channels.

The second term of Eq.C6 is

$$H_2 = \sum_{ls, \Delta n} V_{\Delta n} \lambda_{\Delta n, +} \lambda_{\Delta n, -} \omega^{(l+s)\Delta n} c_{l,+}^\dagger c_{s,-}^\dagger c_{s,-} c_{l,+} = \sum_{ls, \Delta n, \alpha\beta} V_{\Delta n} \rho_{\alpha, +} \rho_{\beta, -} \omega^{(R_{\alpha} + R_{\beta} + l + s)\Delta n} c_{l,+}^\dagger c_{s,-}^\dagger c_{s,-} c_{l,+} \tag{C10}$$

after a mean-field decoupling

$$\begin{aligned}
H_2 &= \sum_{ls, \Delta n, \alpha\beta} V_{\Delta n} \rho_{\alpha, +\rho\beta, -} \omega^{(R_\alpha + R_\beta + l + s)\Delta n} \langle c_{l+}^\dagger c_{l+} \rangle \langle c_{s-}^\dagger c_{s-} \rangle \\
&= V(K) \sum_{ls, \alpha\beta} \rho_{\alpha, +\rho\beta, -} \delta_3(R_\alpha + R_\beta + l + s) \langle c_{l+}^\dagger c_{l+} \rangle \langle c_{s-}^\dagger c_{s-} \rangle + (V(0) - V(K)) \sum_{\alpha\beta} \rho_{\alpha, +\rho\beta, -} \sum_{ls} \langle c_{l+}^\dagger c_{l+} \rangle \langle c_{s-}^\dagger c_{s-} \rangle \\
&= \frac{2}{3} V(K) \sum_{\alpha\beta} \rho_{\alpha, +\rho\beta, -} \cos \left(\theta_1 + \theta_2 + \frac{2(R_\alpha + R_\beta)\pi}{3} \right) + const. \tag{C11}
\end{aligned}$$

This is the Hartree term for inter-MBZ-corner interaction. When the orbital weight ρ_α is polarized to B_5 ($\alpha = 0$), this term is maximized for $l + s \equiv -(\alpha + \beta) \equiv 0 \pmod{3}$. Note that $l + s \pmod{3}$ is associated with the Chern number. So this term penalizes $C = 0$. As soon as the orbital weights shift to B_4 ($\alpha = \beta = 1$), this term penalizes $s + l \equiv 1 \pmod{3}$ instead.

The third line of Eq. C6 becomes

$$H_3 = - \sum_{ll' ss', \Delta n \Delta m} V'_{\Delta n} \lambda_{\Delta n}^{+-} \lambda_{\Delta n + \Delta m}^{+-*} \omega^{(l-l')\Delta n + (s+l')\Delta m} c_{l+}^\dagger c_{s-}^\dagger c_{s'-} c_{l'+} \delta_3(l + s - s' - l') \tag{C12}$$

where

$$V'_n = V(K_i - \bar{K}_{n+i}) = V(K_i + K_{n+i}) = V(K) + (V(2K) - V(K))\delta_{n0} \tag{C13}$$

$$\lambda_{K_i, \bar{K}_{n+i}} = \langle u(K_i) | u(\bar{K}_{n+i}) \rangle = \sum_{\alpha} u_{\alpha}^*(K_i) u_{\alpha}(\bar{K}_{n+i}) = \sum_{\alpha} u_{\alpha}^*(K_0) u_{\alpha}(\bar{K}_0) \omega^{R_{\alpha} n} = \sum_{\alpha} \rho'_{\alpha} \omega^{R_{\alpha} n} \equiv \lambda'_n \tag{C14}$$

At the mean-field level, Eq. C12 reduces to

$$\begin{aligned}
H_3 &= - \sum_{ls, \Delta n \Delta m} V'_{\Delta n} \lambda'_{\Delta n} \lambda_{\Delta n + \Delta m}^{*} \omega^{(s+l)\Delta m} \langle c_{l+}^\dagger c_{l+} \rangle \langle c_{s-}^\dagger c_{s-} \rangle \\
&= - \sum_{ls, \Delta n \Delta m} V'_{\Delta n} \lambda'_{\Delta n} \lambda_{\Delta n + \Delta m}^{*} \omega^{(s+l)\Delta m} \langle c_{l+}^\dagger c_{l+} \rangle \langle c_{s-}^\dagger c_{s-} \rangle \\
&= - \sum_{ls, \alpha\beta} (V(2K) - V(K)) \rho'_{\alpha} \rho_{\beta}^{*} \sum_{\Delta m} \omega^{(s+l-R_{\beta})\Delta m} \langle c_{l+}^\dagger c_{l+} \rangle \langle c_{s-}^\dagger c_{s-} \rangle \\
&\quad - \sum_{ls, \alpha\beta} V(K) \rho'_{\alpha} \rho_{\beta}^{*} \sum_{\Delta n} \omega^{(R_{\alpha}-R_{\beta})\Delta n} \sum_{\Delta m} \omega^{(s+l-R_{\beta})\Delta m} \langle c_{l+}^\dagger c_{l+} \rangle \langle c_{s-}^\dagger c_{s-} \rangle \\
&= \sum_{ls, \alpha\beta} (V(K) - V(2K)) \rho'_{\alpha} \rho_{\beta}^{*} \delta_3(s + l - R_{\beta}) \langle c_{l+}^\dagger c_{l+} \rangle \langle c_{s-}^\dagger c_{s-} \rangle \\
&\quad - \sum_{ls, \alpha\beta} V(K) \rho'_{\alpha} \rho_{\beta}^{*} \delta_3(R_{\alpha} - R_{\beta}) \delta_3(s + l - R_{\beta}) \langle c_{l+}^\dagger c_{l+} \rangle \langle c_{s-}^\dagger c_{s-} \rangle \\
&= \frac{2}{3} \sum_{\alpha\beta} \{ (V(K) - V(2K)) \rho'_{\alpha} \rho_{\beta}^{*} - V(K) \rho'_{\alpha} \rho_{\beta}^{*} \delta_3(R_{\alpha} - R_{\beta}) \} \cos(\theta_1 + \theta_2 - R_{\beta}) + const. \tag{C15}
\end{aligned}$$

This is the Fock term between K_M and \bar{K}_M .

At a large displacement field, although there is significant hybridization between B_5 and B_4 at BZ corners, the density is still predominantly on B_5 orbital. As a simple consideration, consider the extreme scenario where the charge is polarized to the B_5 orbital, $\rho_0 = \rho'_0 = 1$, then

$$H_2 = \frac{2}{3} V(K) \cos(\theta_1 + \theta_2) + const. \tag{C16}$$

$$H_3 = -\frac{2}{3} V(2K) \cos(\theta_1 + \theta_2) + const. \tag{C17}$$

Since $V(K) > V(2K)$, Hartree term dominates. Then $C \equiv l + s = \frac{3(\theta_1 + \theta_2)}{2\pi} \equiv 0 \pmod{3}$ is higher in energy than $C = 1$ and $C = -1$.

Appendix D: Comparison of Fermi liquid and Hall crystal: Hartree Fock energies

We present in Fig. 10 the Hartree-Fock energy difference of the translation symmetry preserving Fermi liquid and translation symmetry breaking Hall crystal for wavevector \vec{G}_M associated with moiré twist angle of 0.77° for $u_d = -36$ meV. As seen, for a range of displacement field energies, the Fermi liquid state is higher in energy than the Hall crystal. As alluded to in the main text, this energy difference is not altogether surprising, as the Hartree-Fock framework is biased towards finding translation symmetry broken (and gapped) phases of matter.

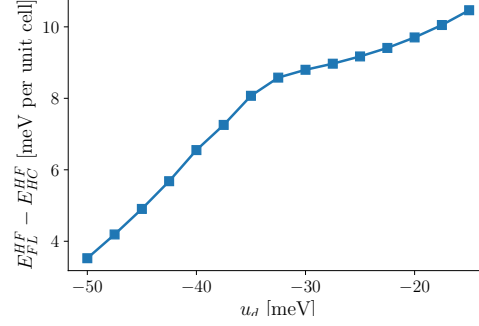


Figure 10. Energy difference of translation symmetry preserving Fermi liquid and translation symmetry breaking Hall crystal for wavevector \vec{G}_M associated with moiré twist angle of 0.77° for $u_d = -36$ meV.